Phase coexistence and pressure-temperature phase evolution of VO_2(A) nanorods near the semiconductor-semiconductor transition

Sudeshna Samanta,[1] Quanjun Li,[2] Benyuan Cheng,[2] Yanwei Huang,[1] Cuiying Pei,[1] Qinglin Wang,[3,4] Yanzhang Ma,[4,5] and Lin Wang[1,*]

[1]*Center for High Pressure Science & Technology Advanced Research, Shanghai, China*
[2]*State Key Laboratory of Superhard Materials, Jilin University, Changchun, China*
[3]*Shandong Key Laboratory of Optical Communication Science and Technology, School of Physics Science & Information Technology of Liaocheng University, Liaocheng, China*
[4]*Center for High Pressure Science & Technology Advanced Research, Changchun, China*
[5]*Department of Mechanical Engineering, Texas Tech University, Lubbock, Texas 79409, USA*

(Received 9 September 2016; published 23 January 2017)

A comprehensive understanding of the physical origins of the phase transition behaviors of transition metal oxides is still complex due to the interplay among competing interactions of comparable strengths tuning their nature. Widespread interest in such phase transitions has motivated explorations of nanocrystalline vanadium dioxide (VO_2) in various forms and a long-running debate persists over the roles played by electron-electron correlation with lattice distortion. External stimuli like pressure and temperature have strong effects on the appearance, stability, and spacial distribution of the high-resistive (HR) and low-resistive (LR) phases accompanying their structural modification. Our comprehensive experiments establish the pressure-induced and thermally driven evolution of phase coexistence in VO_2(A) nanorods. Our experimental evidence supports coexisting HR and LR phases, where compression suppressed coexistence at ∼7 GPa, followed by a semiconductor-semiconductor transition at around ∼10 GPa with the absence of pressure-induced metallization. X-ray diffraction revealed lattice distortion with local microscopic strain inhomogeneity in the nanorods, without any discontinuity in the pressure-volume data. We further investigated the vibrational modes and relaxations of the samples related to their thermal expansions. We also found that the pressure-dependent hierarchy of microstructural densification contributed significantly to the resulting transport properties.

DOI: 10.1103/PhysRevB.95.045135

I. INTRODUCTION

Transition metal oxides (TMOs) are a focus of material research due to their superior physical properties including high-temperature superconductivity, insulator-metal transitions (IMTs), colossal magnetoresistance, etc. In these materials, competing phases often coexist as nano- or microscale domains. The inhomogeneity of these phases alters the intrinsic properties of the individual phases and requires the ability to control the domain structures and phase transitions in them. In TMOs, such electronic correlations strongly affect their conduction mechanisms, while in some oxides their lattice degrees of freedom also play a crucial role. This is the case in vanadium oxide (VO_2) [1], a typically representative TMO where a structural transition coincides with a first-order IMT accompanied by the opening of a midinfrared optical gap [2,3] which indicates strong coupling between the electron-electron and electron-lattice interactions driving the IMT. In this context, external perturbations like temperature (T), pressure (P), or both have the ability to control the phase inhomogeneity in VO_2, where insulator-metal or semiconductor-semiconductor transitions with T [2,4–7] or P [8–12] are long debated issues.

To date, studies on VO_2, temperature-dependent phase inhomogeneity have been limited to thin films and nanowires and nanobeams. High conducting states in the form of nanoscale metallic puddles within an insulating host matrix [4–7,13] have been found in the thin films and nanowires, whereas self-organized, energetically favorable, and alternating spacial arrangements of insulating and metallic domains have been observed in nanobeams [4–7]. The mobile charge carriers experience strong interactions with competing phases and make spacial current paths highly inhomogeneous [14] and percolative [4–7]. Nanoscopic spacial inhomogeneity comprises low-resistive (LR) and high-resistive (HR) volume phase fractions [4–7,15,16] and can tune electrical transport properties over coexisting phases across IMTs, where the dynamic responses of these individual electronic phases are averaged in macroscopic studies. In this paper, we probe the phase coexistence of such LR and HR phases in a VO_2 polymorph, VO_2(A) nanorods, at high pressure (HP) while continuously tuning its crystal structure.

VO_2(A) is a TMO at ambient pressure and undergoes a thermally driven IMT at $T_C \simeq 162\,^{\circ}$C from a low-T tetragonal phase (LTP-A_L) to a high-T body-center tetragonal phase (HTP-A_H) [17–19]. Moreover, reports on VO_2(A) nanorods [20–22] strongly suggest they have coupling of electronic and structural phase transitions (at $210\,^{\circ}\text{C} > T_C$) weaker than that of VO_2(M) [2] with a similar band gap $\Phi \sim 0.6$ eV [23]. The relationship between the IMT and the accompanying structural changes in VO_2(A) nanorods drives pressure-induced metallization (PIM) and amorphization (PIA) at 300 K [24]. The emergence of a T- or P-induced "metal" phase in VO_2(A) deviates from a conventional metal, and while P-dependent optical data shows the band gap closing [24], the activated kinetics from dc electrical transport ($T > T_C$) and band structure calculations [22] support a semiconductor-semiconductor ($A_H \rightarrow A_L$) transition rather than an IMT.

*Corresponding author: wanglin@hpstar.ac.cn

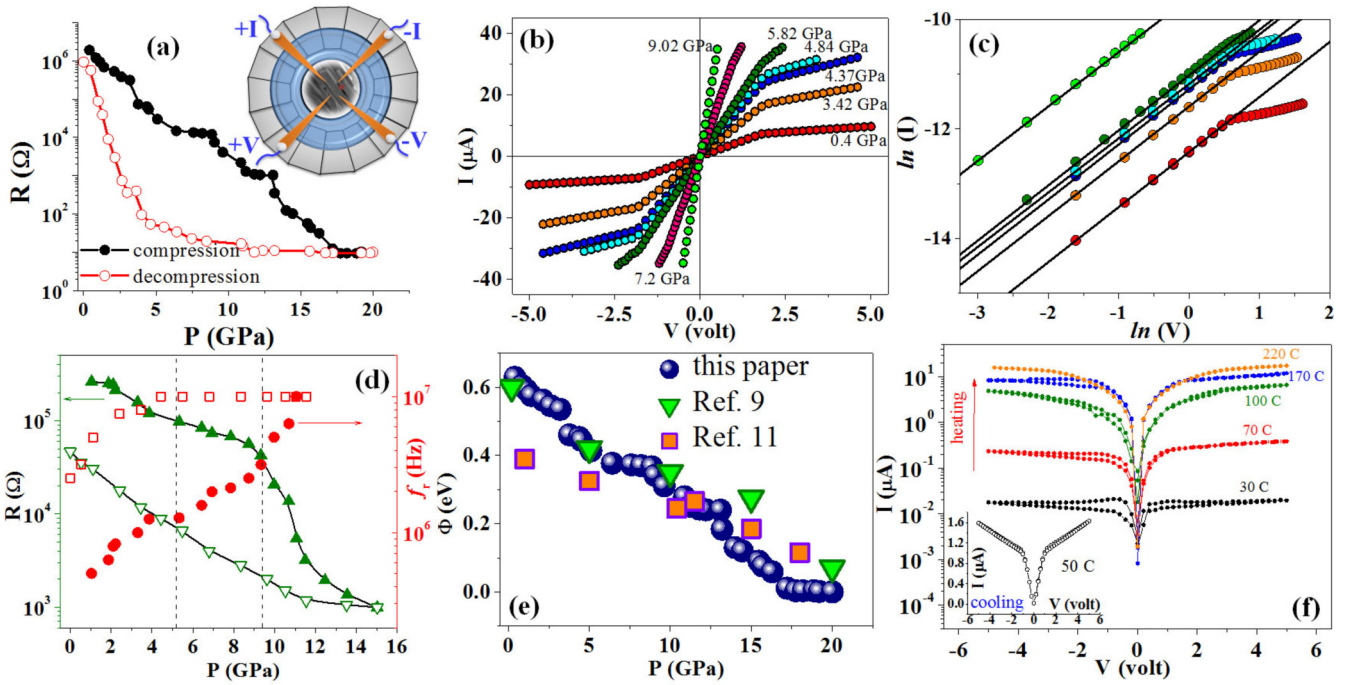

FIG. 1. (a) P dependence of R measured in the four-probe configuration (inset). (b) I-V characteristics at different P. (c) ln(V)- ln(I) data to focus on the inhomogeneous conduction mechanism with P (see text). (d) Variations of total R and f_r with P measured by ac impedance spectroscopy (solid and open symbols are for compression and decompression, respectively). (e) Pressure dependence of the band gap Φ extracted from R-P data. (f) Temperature-dependent I-V characteristics show thermal hysteresis for $T \leqslant T_C$ and vanish for $T > T_C$; inset shows the thermal reversibility of the nanorods.

Anisotropic compression of the lattice constants and drastic deformations and multiple rotations of the VO6 octahedra explain these transition mechanisms [24]. These pressure-induced solid-solid phase transitions are generally highly hysteretic and involve the propagation of multiple domains resulting in structural distortions [2,25] and, therefore, offer an efficient way to organize metal-insulator microstructures for studying phase coexistence under HP.

In this work, we not only observed resistance (R) evolution with P in VO_2(A) nanorods but also extensively studied their phase-coexistence phenomena, simultaneously recording of the dc current-voltage (I-V) characteristics by constructing four-probe geometry [inset Fig. 1(a)] [26]. We used synchrotron x-ray diffraction to probe qualitative structural information and simultaneously explored the thermal expansion of VO_2(A) nanorods under HP and high-temperature (HT) Raman spectroscopy. Using scanning electron microscopy (SEM), we observed morphological integrity and multiple local orderings of the nanorods, which explained their electrical transport mechanism. Combining the results of our multidirectional studies, we present a P-T phase diagram for VO_2(A) nanorods that encompasses their phase transitions.

II. EXPERIMENTAL

VO_2(A) nanorods were synthesized by a hydrothermal method using high-purity V_2O_5 and oxalic acid as reagents, as previously described [24]. Briefly, 0.2275 gm V_2O_5 was added to 0.393 75 gm oxalic acid and 100 ml distilled water. The mixture was stirred continuously until a clear orange transparent solution formed. The precursor solution of 50 ml was placed in an autoclave at 270 °C for 24 h. Finally, after cooling and washing, the product was dried for 2 days in a vacuum freeze dryer. Scanning electron microscopy (SEM) and energy dispersive x-ray spectroscopy were used to confirm its rod-like morphology and the chemical composition, respectively. The transmission electron microscope images revealed that the nanorods had a preferred crystallographic orientation along the [110] direction [24] with a large length/diameter (L/D) ratio. As a result, we expect to observe anisotropic pressure effects in the axial and radial directions.

A symmetric diamond-anvil-cell (DAC) was used for our experiments to generate high pressure on the nanorods. A stainless steel gasket was preindented with a 51-μm thickness, followed by laser-drilling the central part to make a 150-μm-diameter hole. Cubic boron nitride was pressed inside the steel gasket and drilled again to insulate it for transport measurements [26]. Programmable current and voltage sources were used to carry out electrical transport measurements. Silicone oil was used as a pressure-transmitting medium (PTM) for the x-ray diffaction (XRD) and Raman spectroscopy experiments only. SEM studies and electrical transport measurements were conducted without any PTM.

At room temperature, angle-dispersive XRD data were collected at the Shanghai Synchrotron Radiation Facility (SSRF), Beamline 15BLU1 with wavelength $\lambda = 0.6199$ Å, and intensities with 2θ patterns were recorded. Pressure was measured by the ruby fluorescence method [27]. The diffraction data were analyzed using FIT2D software. XRD

diffraction patterns were collected using a Mar165 CCD detector. Reitveld refinement analyses were performed using GSAS software to identify the crystal structures and to study the pressure dependence of the lattice parameters [26].

Pressure-induced and temperature-dependent Raman spectra were collected by in-house Raman facilities (inVia Renishaw Raman spectrometer) with a 532-nm exciting laser with 2400 g/cm grating. For *in situ* temperature-dependent studies, the sample was heated for 20 min to reach thermal equilibrium at each temperature where the holding time was about 5 min.

III. RESULTS AND DISCUSSION

A. Phase coexistence under high pressure

To observe the effect of pressure, we conducted *in situ* electrical resistance measurements inside a diamond-anvil-cell (DAC). Figure 1(a) shows the P dependence ($\leqslant$20 GPa) of the nanorod electrical resistance $R(P)$. R decreased by 5 orders of magnitude with increasing P in the entire pressure range. Accurate estimation of the nanorods' assembly thickness was difficult, so we calculated the ratio as $R_p = R(P = 0\ \text{GPa})/R(P = 20\ \text{GPa})$ and the result was $\approx 1.2 \times 10^6$. The R_p is 1 order of magnitude higher than the reported values of VO_2 [9,11]. Above 17 GPa, resistance became almost pressure independent. We discovered that several short-range resistance valleys accompanied the reduction of R from a HR to LR state, which is a very new observation on VO_2 [9,11]. In these valleys, R changed the slope with P and ultimately saturated to a LR state of $P \approx 20$ GPa. We avoided PIA above 25 GPa [24] to check if this sample state was reversible under P and decompression, and it almost returned to its original value, albeit with a slower rate of resistance with pressure. The hysteresis of our R-P data signifies a different amount of LR and HR phases for compression and decompression even though it was reversible. The nature of the transition corresponding to the electronic phase of VO_2(A) should have a double-well potential as a function of pressure. The HR phase and the LR phase are nearly degenerate and hence bistable, giving rise to a pressure-induced hysteresis loop. Scanning P at a fixed temperature corresponded to an isothermal change of potential from one stable state to other, and a comparable effect was revealed by the temperature scan. A huge resistance ratio ($>10^6$:1) observed between these two stable states is unreported but an electric-field-induced low-R phase has been previously achieved in VO_2 thin film, where surface charge accumulation was accompanied by collective lattice distortion leading to the transition [28].

Our simultaneous tracking of dc current-voltage (I-V) characteristics with P, confirmed the existence of distinct conductivity regimes in nanorods at 300 K, as shown in Fig. 1(b). To illustrate the mechanism, we plotted $\ln(I)$ vs $\ln(V)$ in Fig. 1(c) and fitted straight lines (solid lines) with the equation $I \propto V^s$ in two voltage regions across a threshold voltage V_{th}. Even at ambient pressure, the HR ($s \approx 1$) and LR ($s \approx 0.3$) states coexisted. With increasing P, the V_{th} vanished, the I increased sharply above 7.0 GPa [Fig. 1(b)] and single phase conduction processes dominated. In the HR phase, resistance was strongly pressure dependent [see Fig. 1(c)]. However, the LR phase resistance was nearly pressure independent. These results strongly support that inhomogeneous current conduction paths occur during compression and decompression. The dynamic evolution of metallic and insulating volume phase fractions was previously observed in VO_2 strained thin film [15] during an IMT.

To gain further insight, we conducted P-induced ac impedance spectroscopy (see results in Fig. 1(d) [26]). At ambient pressure, we observed one single semicircle (Z'-Z'') with a slightly nonideal (non-Debye) relaxation frequency response [26]. With increasing pressure, the semicircles shrunk and the center of each semicircle shifted towards lower values of the real Z axis [26]. Figure 1(d) shows the sharp decrease in the total R when $P > 8.0$ GPa. Our resistance values from both dc and ac measurements were fairly compatible. Considering the parallel-plate capacitor R-CPE model, we calculated the relative permittivity (ϵ_r) and relaxation frequency (f_r) of the nanorods [26]. Figure 1(d) shows the f_r increases sharply above 8 GPa and finally reach our instrumental limit (10 MHz). The bulk conduction process mainly dominates the ac electrical transport and depends on the interior mechanisms of the nanorods. Our results predict the emergence of a high conducting state with carriers having low relaxation time τ, i.e., large f_r. If we consider f_r follows the Arrhenius law, the activation energy E_a decreases with increasing P are as high as -14.62 meV/GPa for $P > 8$ GPa, favoring a charge-carrier transport process in the entire region [26].

We can adopt a basic phenomenological model based on two-phase coexistence; one is a HR phase and the other is a LR phase with resistances R_{HR} and R_{LR}, respectively. The m_f is the total volume fraction of the phase, where R_{LR} represents the "mobile" (or depinned) fraction of the phase that will effectively contribute to the transport. The applied voltage and P both can enhance the conducting volume phase fraction. At room temperature, the applied pressure cannot create any new minority LR phase but increases its mobile phase fraction m_f. Under this framework, the observed R can be written as

$$R = \frac{R_{HR}R_{LR}}{(1 - m_f)R_{LR} + m_f R_{HR}}. \quad (1)$$

We found the temperature dependence of $m_f = 1/[1 + m_{f0} \exp(\Delta/k_B T)]$, where Δ is the activation energy [15]. The prefactor m_{f0} could have complex dependencies of P and increases with P. Though it is difficult to write the specific dependence of m_f with P, we expected that there must be a depinning pressure for the pinned minority LR phase. Hence, the observed resistive transition can be identified as a pressure-driven percolation-type transition between two states with coexisting phases and is described later. We roughly estimated the band gap Φ with P from the R-P data and compared it with the reported values of VO_2 [9,11], as shown in Fig. 1(e); Φ almost closed at $P > 17$ GPa but is not a definitive signature of VO_2(A) metallization.

B. Temperature-driven phase transition

We reproduced the temperature-driven phase transition [22] in nanorods and show their dc I-V characteristics in Fig. 1(f) for selected T. The I increases by 3 orders of magnitude with increasing T at ambient P, reflecting a phase transition

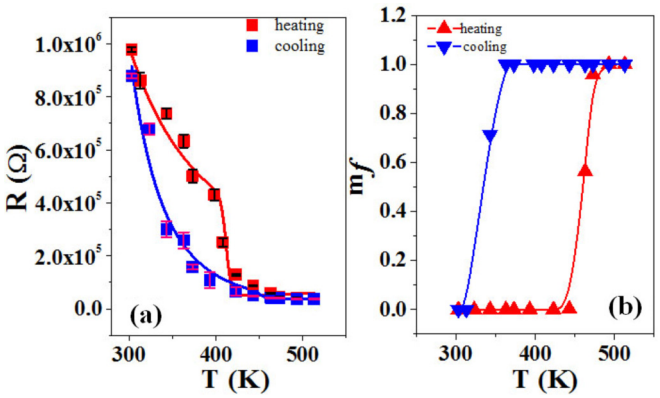

FIG. 2. (a) Temperature dependencies of R where solid lines represent the model fit with Eq. (1). (b) Variation of the LR phase fraction m_f at ambient pressure. Near the transition, m_f changes drastically and is accompanied by significant changes in resistance.

from HR to LR states at $T_C = 170\,^{\circ}$C. The hysteresis we observed in the I-V data for $T \leqslant T_C$ is a definitive signature of multiple simultaneous phases with different conductivities. As T increased, the LR phases started to grow over the HR phases and hysteresis vanished at $T > T_C$. The heating and cooling processes were reversible and matched earlier single VO_2(A) nanowire experiments well [22]. We estimated the approximate carrier density $n_c \sim 1 \times 10^{17}/\text{cm}^3$ with Hall mobility ~ 1 cm^2/Vs [29] and it was 2 orders of magnitude lower than the carrier density of VO_2(M) at ambient conditions. At 220 °C, n_c increased to $5 \times 10^{20}/\text{cm}^3$ but was still too low to be a conventional metal equivalent. From the temperature dependence of R in Fig. 2(a), we obtained the temperature evolution of m_f using Eq. (1) as plotted in Fig. 2(b). The value of the activation energy was $\Delta \sim 4.239$ eV, where at and above the transition $m_f \to 1$. The cooling and heating processes may modify the exact fraction of the two coexisting phases leading to a difference in m_f during thermal cycling. At room temperature, the LR phase with $m_f < 10^{-3}$ was mainly surrounded by a HR phase, an increase of temperature enhanced the LR phase fraction m_f, and the current increased significantly.

First-principle calculations [22] revealed the presence of two different V-O bond distances of 1.703 and 1.695 Å, associated with the A_L and A_H phases, respectively, with distorted VO6 octahedra. Across the thermally-driven structural phase transition, the bond distances of the V − V pairing modification occurred, which drove A_L and A_H to become indirect-band gap semiconductors with band gaps of 1.12 and 0.75 eV, respectively.

C. Pressure-induced and temperature-driven Raman spectroscopy

To connect electronic and structural contributions to the carrier transport mechanism, we performed HP and HT Raman spectroscopy. We calculated the isothermal $[\gamma_{iT} = \frac{\beta_0}{\omega_i}(\frac{d\omega_i}{dP})_T]$ and isobaric $[\gamma_{iP} = -\frac{1}{\alpha\omega_i}(\frac{d\omega_i}{dT})_P]$ mode Grüneisen parameters, where β_0 and α are the bulk modulus and thermal expansion coefficient, respectively; and γ_{iT} and γ_{iP} were used to separate the implicit (volume dependent) and explicit/true anharmonicity (phonon-phonon anharmonic interactions) contributions of the Raman active modes of the VO_2(A) nanorods. We avoided PIA and observed completely reversible Raman active modes, under independent compression and heat, or the application of both [26]. Out of 15 phonon modes at 300 K, we selected the most intense as spectroscopic markers and studied their dependencies with the simultaneous application of P and T: two low-frequency modes ($\omega_{v1} = 162\,\text{cm}^{-1}, \omega_{v2} = 215\,\text{cm}^{-1}$) and two high-frequency modes ($\omega_{o1} = 890$ cm^{-1}, $\omega_{o2} = 940$ cm^{-1}). Figure 3(a) shows the variation of one selective mode ω_{v1} in the P-T plane, whereas the rest of the modes show similar dependencies; ω_{v1} and ω_{v2} correspond to the V mass, and the ω_{o1} and ω_{o2} modes relate to the reduced V and O masses, providing information for the V-V and V-O motions, respectively [10]. The observed shifts of ω_{o1} (2.72 cm^{-1}/GPa) larger than those of ω_{v1} (1.16 cm^{-1}/GPa) with P confirmed the reconstruction of the V-O lengths and distortions of the VO6 octahedra [24] along the c_R axes of the nanorods, as VO_2(A) nanorods were highly oriented along the [110] direction [24] and the surface stresses strongly influenced the spacial distribution of the individual nanorod phases.

We calculated γ_{iT} and $\beta_0 = 213$ GPa [9] for the four modes shown in Fig. 3(b). The VO_2(A) nanorods show a positive thermal expansion with T and decrease significantly across the phase transition. Assuming a quasiharmonic approximation at 300 K $\ll \theta_D \simeq 750$ K (Debye temperature of VO_2 [30]), our estimated $\alpha_c = \frac{1}{V_m\beta_0}\Sigma C_i\gamma_i$, where C_i is the specific heat and V_m is the molar volume, is $\simeq 5 \times 10^{-6}$ K^{-1}. The α_c is six times smaller than an earlier reported [30] value of 25–30 $\times 10^{-6}$ K^{-1} along the c_R axis, due to a considerable contribution from explicit anharmonicity. The implicit parameter $\eta = \gamma_{iT}/\gamma_{iP}$ measures the relative contribution of two anharmonicities and is shown in Fig. 3(c), where the variation of γ_{iP} at 10 GPa is shown in the inset. For both modes, $0 < \eta < 0.5$, which implies most of the contribution is due to explicit anharmonicity. The Raman modes became weaker and their thermal reversibility signified a temperature-driven reversible structural transition from HR-A_L to LR-A_H, as shown in Fig. 3(d). Until now, there have been no reports on the thermal expansion of the VO_2 family under P.

At 300 K under HP, though we achieved a LR (high conducting) state, the Raman modes survived ($P \simeq 25$ GPa), supporting the phase coexistence of HR islands in a high-density LR phase until 25 GPa. Raman spectroscopy is a local probe and thus it is hard to confirm pure metallization throughout the whole sample due to the spacial distributions of domains with varying conductivities along the axis of the nanorods. We found that, when we targeted the laser spot at different positions, some of the intense Raman modes disappeared suddenly with signatures of growing conducting phases. An earlier study observed similar behavior in VO_2 nanowires [7]. Scanning near-field optical microscopy (s-SNOM) in VO_2 microcrystals [31,32] and nanoimaging in thin films [13] also confirmed a sequence of formation, gradual growth of periodic metallic domains, and their spacial evolution in a nanometer scale to achieve a fully metallic state. We predict that similar phenomena occur in nanorods when stressed. Due to the rodlike geometry, the surface stress fields [33] ($\sigma_s = 4\Sigma l/A$, where Σ, l, and A are surface

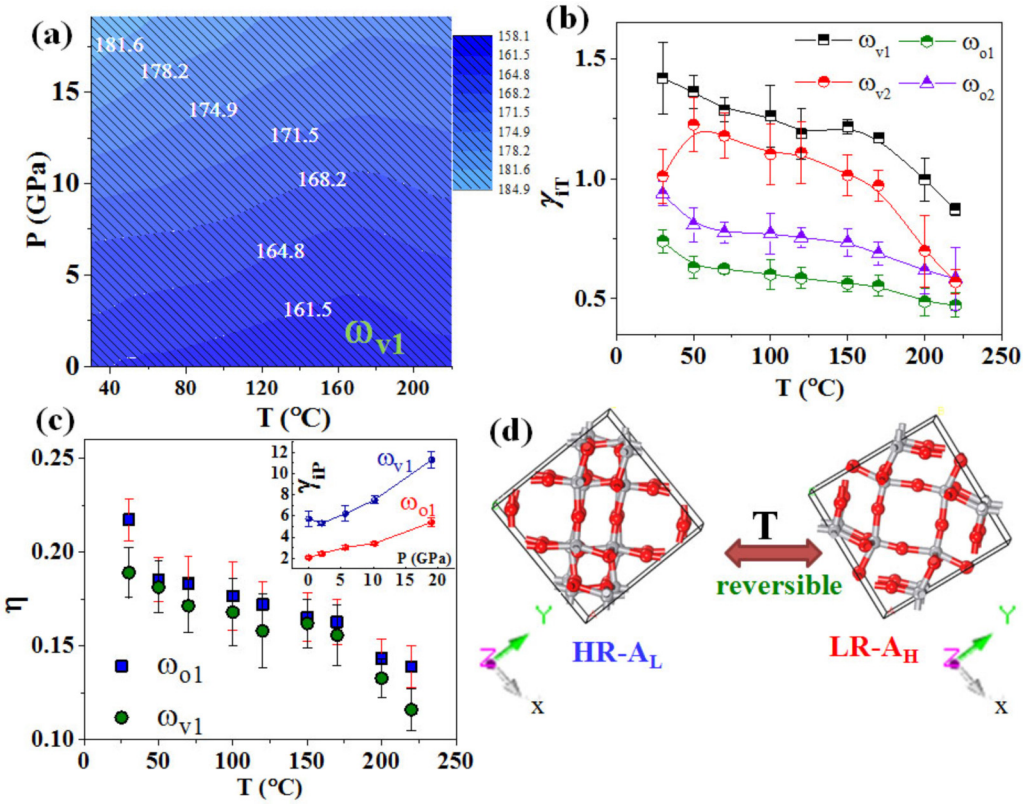

FIG. 3. (a) P and T dependencies of selective Raman mode ω_{v1}. (b) Variation of γ_{iT} with T for four selective modes. (c) The implicit fraction $\eta = \gamma_{iT}/\gamma_{iP}$ for ω_{v1} and ω_{o1} with T at 10 GPa. Variation of γ_{iP} with P (inset). (d) Crystal structures showing a reversible IMT with T. The crystallographic c axis is along the Z direction.

stress component, length, and area of the NR, respectively) generated by compression are highly inhomogeneous and complicated, and when induced compressive stress exceeds the critical σ_s and a phase transition occurs. These phenomena are qualitatively consistent with our synchrotron XRD spectra in VO_2(A) nanorods.

D. Crystal structure and microstructural densification

The HP synchrotron XRD is shown in Fig. 4(a) up to 30 GPa and until PIA [24]. The ambient phase is a tetragonal $P4/ncc$ structure. No obvious changes in peak positions were observed, whereas the (211), (311), and (114) reflections almost disappeared at around $P \geqslant 14$ GPa. Moreover, the (211) peak shifted first to a lower 2θ value at the same P and started to move towards a higher 2θ value again with increasing P. After Reitveld refinements, we observed no discontinuous volume change, which ruled out the presence of a first-order-phase transition with P. Similarly, Yao *et al.* [17] observed two XRD patterns for a LTP and a HTP, where the (211) and (311) reflections at 200 °C (HTP) almost disappeared due to rotational shifts of the V atoms around the c axis during the phase transition. At 300 K, it is possible that a HP phase ($VO_2(A)_{HP}$) similar to the HTP formed at much lower $P \simeq 14$ GPa and has characteristics with unidentified crystallographic orientations. At the same pressure, a HP structural phase of VO_2 was observed where the appearance of a new distorted monoclinic insulating phase remained undetermined [9,10].

We propose that a mechanism of hierarchical densification/closed-packed ordering of the nanorods explains the emergence of the high conducting LR phase [Fig. 1(b)] at much lower P. We collected SEM images of the decompressed samples marked at different P points, as shown in Fig. 4(b). As

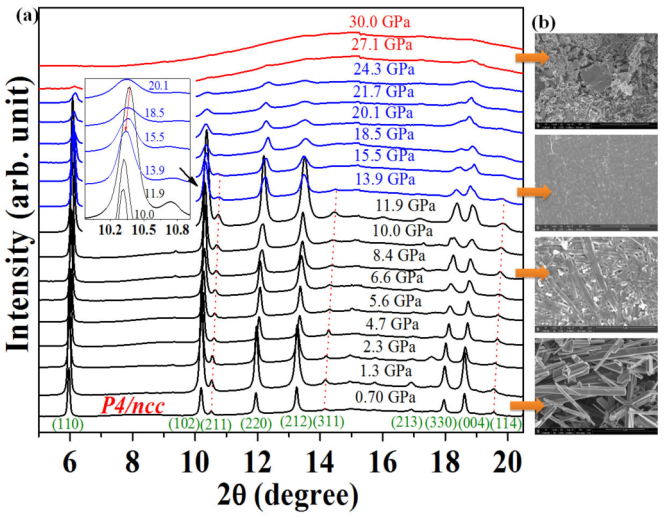

FIG. 4. (a) XRD patterns for VO_2(A) at a few selective pressure values, where the ambient phase is a tetragonal $P4/ncc$ structure. (b) SEM pictures were taken for decompressed samples; compression pressures are marked with arrows.

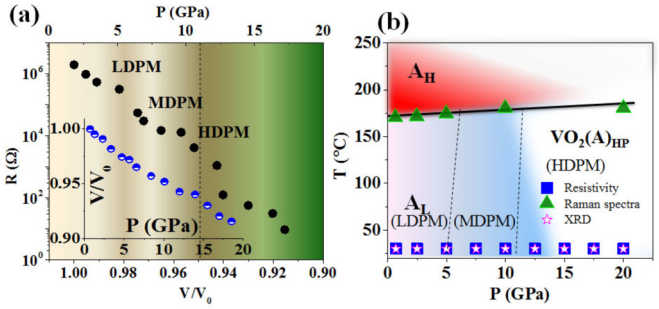

FIG. 5. (a) R vs V/V_0 shows the volume reduction related to the densification processes. The inset shows P vs V/V_0 derived from XRD refinements. (b) In the P-T phase diagram of VO_2(A), the data from electrical transport, Raman spectroscopy, and XRD measurements are summarized. The high-pressure, low-resistive $VO_2(A)_{HP}$ belongs to a HDPM form up to 20 GPa before PIA.

P increased, the nanorods aligned themselves more densely and broke into small pieces to maximize filling the void spaces. At low $P \sim 0$–5 GPa, the nanorods accommodated the applied pressure and formed low-density packed microstructures (LDPMs). The LDPMs transformed into medium-density packed microstructures (MDPMs) at about 5–8 GPa. For both the LDPM and MDPM states, R decreased (I increased) significantly due to increased connectivity among the nanorods. Figure 5(a) shows the variation of R with normalized volume V/V_0. The LDPM to MDPM transformation is due to a change in packing density. A slight rotation or distortion of the structures may have occurred, but its contribution to the volume reduction is negligible. Figure 5(a)(inset) shows the small variation in the lattice parameters [26] and volume observed in this pressure range.

Resistance changed by 2 orders of magnitude with a 4% change of volume from ambient conditions to MDPMs. Nonlinear I-V curves carried combined information about microstuctural densification and the quality of the phases. Up to MDPMs, it is very difficult to decouple the nonlinearity contributions in the I-V curves, which have electronic and microstructural origins with no obvious structural change [see inset Fig. 1(b)]. By accumulating other results around $P \geqslant 10$ GPa, we suggest that the nanorods started to form high-density packed microstructures (HDPMs) and the lattice started to distort to accommodate much higher pressure. The interatomic bonds modified and the rotation or distortion of the crystal were obvious mechanisms here. The MDPM to HDPM transformation comprised volume shrinkage and lattice modification under P and the HDPM continued until it lost crystallinity above 25 GPa. In the HDPM region, the same volume reduction (4%) caused a decrease of R by 4 orders of magnitude. Hence, we confirm that our observed LR state [Fig. 1(a)] appears at a critical pressure, $P' > 10$ GPa, and has a HP origin. In earlier studies, a P-induced densification mechanism and a strong coupling among the nanorods were observed around 8–10 GPa in InAs [34] and Si [35] nanowires, where the disappearance of low-frequency modes and the increased intensity of high-frequency Raman modes were also observed, respectively. These predictions of improved alignment and the growth of bundle size in a particular direction with increasing P are established in Fig. 4(b).

E. P-T phase diagram

$VO_2(A)_{HP}$ is a LR phase that contains conducting volume phase fractions larger than those found under ambient conditions. In our case, the survival of the Raman modes until 25 GPa and their position-sensitive disappearance supports the coexistence of conducting and nonconducting phases. Recently, Zhang *et al.* [11] observed a semiconductor-semiconductor transformation in VO_2(M) that closely resembles our results with similar $E_a \simeq= 0.28$ eV at 10 GPa. The carrier density $n \propto e^{-E_a/k_BT}$ estimated for nanorods is $n_{NR} \sim 3 \times 10^{19}$ cm^{-3} at 10 GPa, which is 3 orders of magnitude lower than the bulk n for VO_2 [36] and is far from PIM.

An estimation of Φ at HP can be erroneous [9] as it neglects grain boundary conduction contributions and electron mobility μ. This region is indeed a HDPM phase in our case; the grains are compact here and μ increases rapidly for the nanorods [11], which reduces R by a few orders of magnitude above 10 GPa without changing n_{NR} significantly. Two valleys in our R-P data correspond to two different transformations (LDPM $\rightarrow$ MDPM $\rightarrow$ HDPM) of three densification processes. Finally, for $P \simeq 30$ GPa, the nanorods lose their crystallographic information along with their microstructural identity. Hence, $VO_2(A)_{HP}$ could be another semiconductor with higher n_c, which differs from metal significantly. Recently, another polymorph of VO_2, VO_2(B) nanosheets, remained semiconducting with poor electrical conductivity before and after the PIA process [37], which supports our observations. Detailed investigations on the local structure of VO_2 by HP x-ray total scattering experiments followed by atomic pair distribution function [12] showed that the V-V_1 dimerization was not suppressed under compression up to 22 GPa. The V-V_1 bond distance remained distinguishable up to 22 GPa and was not correlated with any change of electronic properties in this pressure range. They observed a conductive transformation around 13 GPa which also supports our observations. Our results clearly suggest a semiconductor-semiconductor transition and appear to be linked with band-gap modification. We unambiguously determined that a pressure-induced HR-LR transition from $VO_2(A) \rightarrow VO_2(A)_{HP}$ significantly differs from the temperature-driven transition from $A_L \rightarrow A_H$.

In the HP regime, the LR phase supports the formation of more homogeneous, highly connected domains available for the conduction processes. To find the volume phase fractions of our conducting and nonconducting phases, we assumed that the nanorods were two-component binary mixtures with a total volume of $V = \phi_1 V_1 + \phi_2 V_2$ and $\phi_1 + \phi_2 = 1$, where conducting (nonconducting) volumes V_1 (V_2) have a percentage of ϕ_1 (ϕ_2). The volume phase fraction of the conducting phase is $\nu = -\frac{V-V_2}{V_2-V_1}\frac{V_1}{V}$. Using the Murnaghan equation of state (EOS) with β_0 and our transport data of $P_1 \simeq 7$ GPa gives $V_2 = 0.97V_0$. Combining XRD and Raman data, we calculated that $V_1 = 0.92V_0$ at $P_1 \simeq 20$ GPa. Our experimental transition pressure $\simeq$10 GPa corresponds to a critical volume fraction for the conducting phase $\nu_c \simeq 0.28$, which is very close to $\nu_{cP} \simeq 0.29$ from the continuum percolation model [38]. With ν_{cP}, the calculated percolation volume fraction is

$V_c = (\frac{v_c P}{V_1} + \frac{1-v_c P}{V_2})^{-1}$. The V_c in the EOS predicts the critical pressure as $P_c \simeq 10.6$ GPa, which interestingly validates our estimation. Surprisingly, this P_c was previously marked as the critical pressure for metallization [10] and isostructural metallic [39] or transient monoclinic-metallic [40] phase in VO_2. We draw a P-T phase diagram for VO_2(A) nanorods in Fig. 5(b). This phase diagram summarizes all our results and demonstrates the coupled mechanisms between electrical transport and structural transition, along with their microscopic information under HP, finding that their rodlike morphology is unsustainable under compression. A similar irreversible phase transformation was recently reported in TiO_2 nanowires [41] too, where no wire shape was preserved upon compression.

IV. CONCLUSIONS

In conclusion, we observed phase-coexistence phenomena in VO_2(A) nanorods, which establishes a semiconductor-semiconductor phase transition upon compression at a percolation threshold pressure of ∼10 GPa. Our analysis suggests that complete metallization while retaining an intact crystal structure and microstructures is unachievable. We believe that the balance between small (atomic)-scale and large (domains)-scale interactions strongly affects the pressure-induced phase transition in one-dimensional systems and competing phases rule the nature of their electrical conductivity. Apart from demonstrating phase-coexistence phenomena, we also employed scanning electron microscopy to probe the modification in the local nanorod microstructures and combined this with high-pressure and high-temperature vibrational Raman spectroscopy to present a phase diagram of VO_2(A) nanorods. The relevance of surface stress variation and the dynamic evolution of insulating (or semiconducting) or metallic domains deserve deeper and careful investigations, along with single nanowire measurements under extreme conditions.

ACKNOWLEDGMENTS

Part of the work was performed at the BL15U1 Beamline, Shanghai Synchrotron Radiation Facility (SSRF), China. We would like to acknowledge support from Ke Yang, Shuai Yan, and Aiguo Li from the SSRF. This work was supported by the NSAF (Grant No. U1530402). L.W. acknowledges support from the Programme for New Century Excellent Talents in University (Grant No. NCET-10-0444) and the "Science Challenging Program (Grant No. JCKY2016212A501)."

S. Samanta and Q. Li contributed equally to this work.

[1] J. B. Goodenough, Annu. Rev. Mater. Sci. **1**, 101 (1971).
[2] F. J. Morin, Phys. Rev. Lett. **3**, 34 (1959).
[3] J. B. Goodenough and H. Y-P. Hong, Phys. Rev. B **8**, 1323 (1973).
[4] J. Cao, E. Ertekin, V. Srinivasan, W. Fan, S. Huang, H. Zheng, J. W. L. Yim, D. R. Khanal, D. F. Ogletree, J. C. Grossman, and J. Wu, Nat. Nanotechnol. **4**, 732 (2009).
[5] J. I. Sohn, H. J. Joo, D. Ahn, H. H. Lee, A. E. Porter, K. Kim, D. J. Kang, and M. E. Welland, Nano Lett. **9**, 3392 (2009).
[6] J. Wei, Z. Wang, W. Chen, and D. H. Cobden, Nat. Nanotechnol. **4**, 420 (2009).
[7] J. I. Sohn, H. Jin Joo, K. S. Kim, H. Woo Yang, A-Rang Jang, D. Ahn, H. H. Lee, S. N. Cha, D. J. Kang, J. M. Kim, and M. E. Welland, Nanotechology **23**, 205707 (2012).
[8] E. Abreu, M. Liu, J. Lu, K. G. West, S. Kittiwatanakul, W. Yin, S. A. Wolf, and R. D. Averitt, New J. Phys. **14**, 083026 (2012).
[9] L. Bai, Q. Li, S. A. Corr, Y. Meng, C. Park, S. V. Sinogeikin, C. Ko, J. Wu, and G. Shen, Phys. Rev. B **91**, 104110 (2015).
[10] E. Arcangeletti, L. Baldassarre, D. Di Castro, S. Lupi, L. Malavasi, C. Marini, A. Perucchi, and P. Postorino, Phys. Rev. Lett. **98**, 196406 (2007).
[11] X. Zhang, J. Zhang, F. Ke, G. Li, Y. Ma, X. Liu, C. Liu, Y. Hao, Y. Ma, and C. Gao, RSC Adv. **5**, 54843 (2015).
[12] M. Baldini, P. Postorino, L. Malavasi, C. Marini, K. W. Chapman, and Ho-kwang Mao, Phys. Rev. B **93**, 245137 (2016).
[13] M. M. Qazilbash, M. Brehm, B. G. Chae, P. C. Ho, G. O. Andreev, B. J. Kim, S. J. Yun, A. V. Balatsky, M. B. Maple, F. Keilmann, H. T. Kim, and D. N. Basov, Science **318**, 1750 (2007).
[14] M. K. Liu, M. Wagner, E. Abreu, S. Kittiwatanakul, A. McLeod, Z. Fei, M. Goldflam, S. Dai, M. M. Fogler, J. Lu, S. A. Wolf, R. D. Averitt, and D. N. Basov, Phys. Rev. Lett. **111**, 096602 (2013).
[15] S. Samanta, A. K. Raychaudhuri, X. Zhong, and A. Gupta, Phys. Rev. B **92**, 195125 (2015).
[16] J. M. Atkin, S. Berweger, E. K. Chavez, M. B. Raschke, J. Cao, W. Fan, and J. Wu, Phys. Rev. B **85**, 020101(R) (2012).
[17] T. Yao, Y. Oka, and N. A. Yamamoto, J. Solid State Chem. **112**, 196 (1994).
[18] Y. Oka, T. Yao, and N. Yamamoto, J. Solid State Chem. **86**, 116 (1990).
[19] M. Li, F. Kong, L. Li, Y. Zhang, L. Chen, W. Yan, and G. Li, Dalton Trans. **40**, 10961 (2011).
[20] J. Hou, J. Zhang, Z. Wang, Z. Zhang, and Z. Ding, RSC Adv. **4**, 18055 (2014).
[21] S. R. Popuri, A. Artemenko, C. Labrugere, M. Miclau, A. Villesuzanne, and M. Pollët, J. Solid State Chem. **213**, 79 (2014).
[22] C. Wang, X. Liu, J. Shao, W. Xiong, W. Ma, and Y. Zheng, RSC Adv. **4**, 64021 (2014).
[23] T. C. Koethe, Z. Hu, M. W. Haverkort, C. Schußler-Langeheine, F. Venturini, N. B. Brookes, O. Tjernberg, W. Reichelt, H. H. Hsieh, H. J. Lin, C. T. Chen, and L. H. Tjeng, Phys. Rev. Lett. **97**, 116402 (2006).
[24] B. Cheng, Q. Li, H. Zhang, R. Liu, B. Liu, Z. Yao, T. Cui, J. Liu, Z. Liu, B. Sundqvist, and B. Liu, Phys. Rev. B **93**, 184109 (2016).
[25] S. H. Tolbert, A. B. Herhold, L. E. Brus, and A. P. Alivisatos, Phys. Rev. Lett. **76**, 4384 (1996).
[26] See Supplemental Material at http://link.aps.org/supplemental/10.1103/PhysRevB.95.045135 for detailed information about sample characterization, measurement procedures, impedance spectroscopy, high-pressure-induced and high-temperature-driven Raman spectroscopy, and lattice parameters for VO_2(A).

[27] H. Mao, J. Xu, and P. J. Bell, Geophys. Res.: Solid Earth **91**, 4673 (1986).
[28] M. Nakano, K. Shibuya, D. Okuyama, T. Hatano, S. Ono, M. Kawasaki, Y. Iwasa, and Y. Tokura, Nature (London) **487**, 459 (2012).
[29] A. Srivastava, H. Rotella, S. Saha, B. Pal, G. Kalon, S. Mathew, M. Motapothula, M. Dykas, P. Yang, E. Okunishi, D. D. Sarma, and T. Venkatesan, APL Mater. **3**, 026101 (2015).
[30] G. V. Chandrashekhar, H. L. C. Barros, and J. M. Honig, Mater. Res. Bull. **8**, 369 (1973).
[31] A. C. Jones, S. Berweger, J. Wei, D. Cobden, and M. B. Raschke, Nano Lett. **10**, 1574 (2010).
[32] S. A. Dögnes, O. Khatib, B. T. O'Callahan, J. M. Atkin, J. H. Park, D. Cobden, and M. B. Raschke, Nano Lett. **16**, 3029 (2016).
[33] J. Diao, K. Gall, and M. L. Dunn, Nat. Mater. **2**, 656 (2003).
[34] D. Majumder, A. Basu, G. D. Mukherjee, D. Ercolani, L. Sorba, and A. Singha, Nanotechnology **25**, 465704 (2014).
[35] S. Bhattacharyya, D. Churochkin, and R. M. Erasmus, Appl. Phys. Lett. **97**, 141912 (2010).
[36] W. H. Hosevear and W. Paul, Phys. Rev. B **7**, 2109 (1973).
[37] Y. Wang, J. Zhu, W. Yang, T. Wen, M. Pravica, Z. Liu, M. Hou, Y. Fei, L. Kang, Z. Lin, C. Jin, and Y. Zhao, Nat. Commun. **7**, 12214 (2016).
[38] B. I. Shklovskii and A. L. Efros, *Electronic Properties of Doped Semiconductors* (Springer, Berlin, 1984).
[39] M. Mitrano, B. Maroni, C. Marini, M. Hanfland, B. Joseph, P. Postorino, and L. Malavasi, Phys. Rev. B **85**, 184108 (2012).
[40] W. P. Hsieh, M. Trigo, D. A. Reis, G. A. Artioli, L. Malavasi, and W. L. Mao, Appl. Phys. Lett. **104**, 021917 (2014).
[41] Z. Dong and Y. Song, Can. J. Chem. **93**, 165 (2015).